# Nonreciprocal Wave Propagation in a Continuum-Based Metamaterial with Space-Time Modulated Resonators

Yangyang Chen,[1] Xiaopeng Li,[1] Hussein Nassar,[1] Andrew N. Norris,[2] Chiara Daraio,[3] and Guoliang Huang[1,*]

[1] *Department of Mechanical and Aerospace Engineering, University of Missouri, Columbia, Missouri 65211, USA*
[2] *Mechanical and Aerospace Engineering, Rutgers University, Piscataway, New Jersey 08854, USA*
[3] *Engineering and Applied Science, California Institute of Technology, Pasadena, California 91125, USA*

(Received 14 March 2019; revised manuscript received 20 May 2019; published 21 June 2019)

Breaking reciprocity with spatiotemporal modulation provides an opportunity to design unprecedented optical, acoustic, and mechanical waveguides. A main challenge is to physically realize continuum-based metamaterials whose properties can be rapidly tuned in both space and time at the length and time scales of the propagated waves. We design a tunable elastic metamaterial by embedding in a beam a set of permanent magnets, and placing oscillating electrical coils coaxially adjacent to each magnet. By programming in space and time the ac input of the coils, the magnet-coil effective coupling stiffness is modulated along with the resonance frequency. Distinctly nonreciprocal flexural wave propagation is then experimentally observed. In addition, robust tunability of unidirectional band gaps and wave energy bias are quantitatively analyzed by applying different modulation current amplitudes, material damping coefficients, and modulation frequencies. Both simplified analytical and finite-element-method-based numerical models of the modulated metamaterial are suggested and analyzed in support of the experimental work. Specifically, unidirectional frequency conversions and band gaps due to the second-order mode interactions are discussed for the first time when the large modulation amplitude is implemented. The suggested prototype sheds light on nonreciprocal waveguiding, which could be applied in advanced wave diodes, phononic logic, energy localization, trapping, and harvesting.

DOI: 10.1103/PhysRevApplied.11.064052

## I. INTRODUCTION

The fundamental principle of reciprocity, requiring that wave propagation between two points be symmetric when source and receiver are interchanged, is a cornerstone of several wave processing techniques [1,2]. Recently, breaking reciprocity has been recognized as a means to design unprecedented wave manipulation devices [3–7]. These include diodes, circulators, and topological insulators that can be applied to advanced vibration isolation, signal processing, phononic logic, acoustic communication and energy localization, and trapping and harvesting devices [3,4,8–12]. One way to achieve nonreciprocity is to leverage harmonic generation phenomena taking place in nonlinear materials driven by a sufficiently large signal [6,10,13]. Another way is to introduce an angular momentum bias, disobeying time-reversal symmetry as in media comprising gyroscopes or circulating fluids [5,11]. A third solution to achieve nonreciprocity is the use of dynamic materials with properties that are inhomogeneous in space and changing in time [7,14–24]. Theoretical studies showed that such space-time modulations of the materials' constitutive properties could be induced in photosensitive [25,26], piezoelectric [27–33], magnetorheological [34], and other soft [35] materials. The wave phenomena expected to occur in such dynamic materials were investigated theoretically and numerically and included one-way mode and frequency conversion, one-way reflection and one-way acceleration, and deceleration of elastic and acoustic waves [17–23]. Nonetheless, fabrication has proven particularly challenging. An experimental work was reported when unidirectional wave propagation at isolated frequencies was observed experimentally in a discrete lattice of permanent magnets coupled to grounded electromagnets [24]. In the study, nonreciprocity was achieved by programming the ac input of the electromagnets so that their interaction with adjacent permanent magnets produced space and time modulation of the effective grounding stiffness [24]. This testbed provided experimental evidence of nonreciprocal propagation of mechanical waves at velocities of the order of 3 m/s and over a frequency range of 20 Hz. However, (1) the proposed discrete system is only for concept demonstration at extremely low frequency and difficult for practical

*huangg@missouri.edu

 

one-way wave device application in which continuum-based materials are highly desired; (2) asymmetric frequency responses were only experimentally demonstrated under harmonic excitations, and therefore, information of nonreciprocal wave transmission and reflection are not physically captured.

In this paper, to tackle those challenges, we design and fabricate a dynamic material displaying nonreciprocal effects for genuine elastic waves, in the form of flexural waves in a metamaterial beam. The metamaterial beam includes magnetic electrical coil resonant elements with coupling stiffness modulated in space and in time (see Fig. 1). Spatiotemporal modulation of the coupling stiffness in a pump-wave fashion is realized by properly manipulating electric currents with different phases between electrical coils. Nonreciprocal propagation arises when waves at a certain frequency transmit unperturbed through the metamaterial if incident from one side, while they are scattered and partially frequency converted if incident from the other side. The flexural waves in the metamaterial beam travel at velocities of around 50 m/s and over a frequency range of as high as 0.3 kHz. We experimentally demonstrate the transient nonreciprocal wave propagation and show tunability of the information transfer by varying the modulation current amplitudes, material damping coefficients, and modulation frequencies. We support our experimental findings by combining analytical and multiphysics numerical approaches. We expect that this strategy may open promising avenues for designing nonreciprocal mechanical devices.

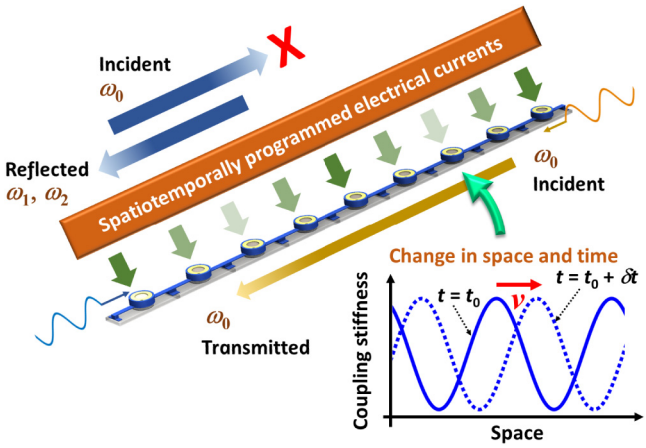


FIG. 1. Physical realization of an elastic metamaterial with inner stiffness electrically modulated in space and in time. The modulation is realized with spatiotemporally programmed electric currents passing through electrical coil-based resonators in the metamaterial. An example of nonreciprocal wave propagation is illustrated in the figure: A wave with the frequency of $\omega_0$ incident from the right to the left will transmit through the modulated metamaterial without frequency conversions, whereas the wave with the frequency of $\omega_0$ incident from the left to the right will be scattered, and multiple frequency conversions will be found in reflected waves.

## II. DESIGN AND MODELING OF THE MODULATED CONTINUUM-BASED METAMATERIAL

The modulated metamaterial comprises an array of magnets and coils periodically distributed over a host beam (see Fig. 2): magnets are rigidly bonded to the beam whereas coils are elastically attached to it through a pair of flexible cantilevers. The assembly allows each coil to oscillate coaxially with its corresponding magnet so that the pair form a resonating dipole (see Fig. 2). The electric current feeding the coils is programmed to tune, within each dipole, the magnetic coupling responsible for the magnet-coil effective coupling stiffness, or equivalently, the dipole resonance frequency. Note that this assembly does not change the effective bending stiffness of the host beam, but rather alters the dynamic response of the attached resonator, which, in turn, results in a time- and space-modulated effective dynamic mass. In order to ensure that the modulation does not act as a source of elastic waves, the absence of net forces between coils and magnets must be guaranteed in the rest state. Accordingly, magnets should be precisely placed at the respective centers

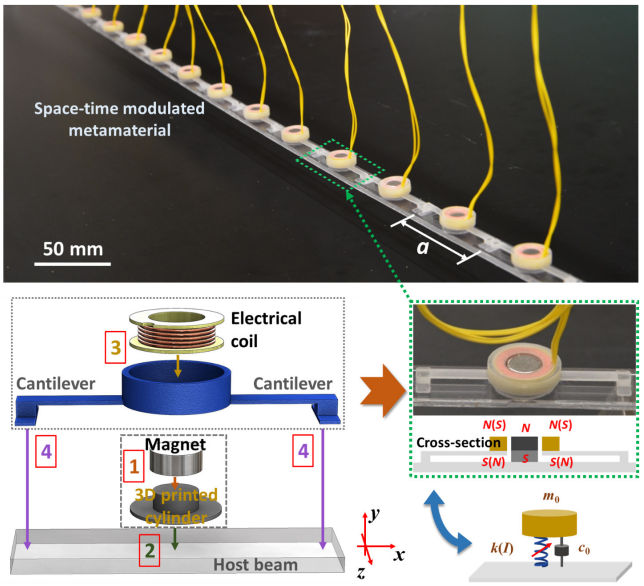


FIG. 2. Design of the modulated metamaterial. The photo shows the fabricated metamaterial samples. The modulated metamaterial comprises an array of magnets and coils periodically distributed over a host beam: magnets are rigidly bonded to the beam whereas coils are elastically attached to it through a pair of flexible cantilevers. The coil-cantilever-magnet system can be understood as a mass-spring resonator with a constant mass $m_0$ and with a tunable spring constant, $k(I)$. The material damping of the cantilever is represented by $c_0$.

of the coils where the magnetic potentials are maximum or minimum. This is achieved using three-dimensional (3D) printed cylinders sandwiched between the magnets and the host beam (see Fig. 2). When the coil deviates from its rest position, it creates an asymmetry in the magnetic field of the magnet and experiences a magnetic force. The sign of the force, that is, restoring or repelling, depends on the sign of the electric current feeding the coil whereas its amplitude, within a linearized regime, is proportional to the magnitude of the current. To characterize the effective stiffness of the magnetic coupling, the induced force is measured by a force gauge at controlled distances separating coil and magnet; observations are then compared to our electromagnetic numerical simulations [see Fig. 3(a)]. The figure indicates that the force-displacement relationship is almost linear for displacement amplitudes ranging from −0.5 to 0.5 mm (shaded area). The vibrations subsequently studied shall be well within that range so that linearity can be comfortably assumed. As a result, the stiffness of the cantilever beam is effectively and linearly modulated by the current. The values of the coupling stiffness induced by different applied currents are also measured and compared to simulated ones [see Fig. 3(b)] and good agreement is observed. In addition, it can be clearly seen that the stiffness changes linearly with the current. Note that when the metamaterial is subject to an incident flexural wave, the moment will also be generated due to the rotational oscillation of the coil in the $x$-$y$ plane. However, the generated moment is very small and can be ignored. With this analysis in mind, the coil-cantilever-magnet system can be understood as a mass-spring resonator with a constant mass $m_0$ and with a tunable spring constant, $k = k_0 + \kappa I$, (see Fig. 2), where $k_0 = l_b^3/6D_b$ is the linear stiffness of the cantilever beam, $D_b$ and $l_b$ are its bending stiffness and length, respectively, and $\kappa = 1760$ N/m·A is the stiffness-to-current ratio obtained from Fig. 3(b). The material damping from the cantilever beams is considered as $c_0 = \beta_0 k_0$, where $\beta_0 = 8 \times 10^{-5}$ s is the Rayleigh damping coefficient. The design, therefore, allows the stiffness of the cantilever beam to triple from $0.5k_0$ to $1.5k_0$ by increasing the current from −0.5 to +0.5 A.

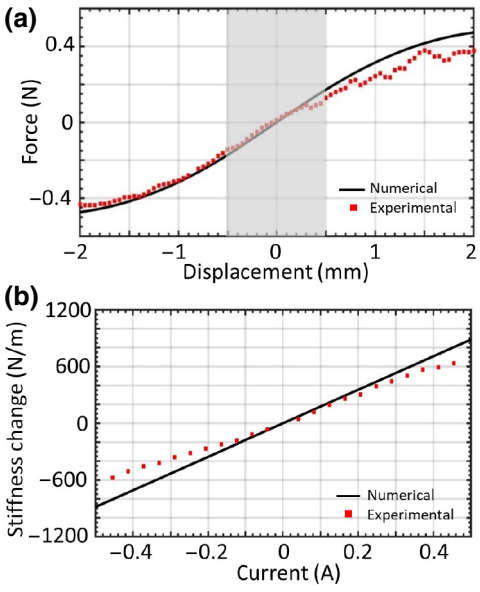


FIG. 3. Characterizations of the modulated coupling stiffness. (a) Experimentally measured and numerically simulated net force induced by the current with different magnet-coil separation displacements, where $I = 0.2$ A. (b) Experimentally measured and numerically simulated coupling stiffness induced with different currents.

The space and time modulation of the metamaterial is realized by applying sinusoidal ac currents $I = I_0 \cos(k_m x \pm \omega_m t)$ in the electric coils to generate a pump wave traveling along the positive or negative $x$ directions. Here $I_0$, $k_m$, and $\omega_m$ represent the modulation current amplitude, modulation wavelength, and modulation frequency, respectively. We focus on experimental observations of nonreciprocal and tunable wave propagation due to Bragg scattering, which requires a dynamic modulation frequency smaller than or comparable with the propagated wave frequency.

We develop a numerical approach to calculate dispersion relations of the modulated metamaterial beam based on the finite element method. In the analysis, components in the metamaterial are modeled as isotropic elastic bodies governed by the Navier-Lamé equation

$$-(\lambda + \mu)\nabla(\nabla \cdot \mathbf{u}) - \mu\nabla^2\mathbf{u} + \rho\frac{\partial^2 \mathbf{u}}{\partial t^2} = \mathbf{F}, \text{ in } \Omega, \quad (1)$$

where $\lambda$ and $\mu$ denote Lamé's constants, and $\mathbf{u}$ and $\mathbf{F}$ represent the displacement and body force vectors, respectively. The body forces induced by electromagnetic interactions are simulated separately based on Ampere's law. In the current model, the induced body forces are assumed to be uniformly distributed in the magnet and electrical coil, which are, respectively, related to the displacements as

$$\mathbf{F} = \mathbf{k}(\langle \mathbf{u} \rangle_c - \langle \mathbf{u} \rangle_m), \text{ in } \Omega_m, \quad (2)$$

$$\mathbf{F} = \mathbf{k}(\langle \mathbf{u} \rangle_m - \langle \mathbf{u} \rangle_c), \text{ in } \Omega_c, \quad (3)$$

where $\langle \cdot \rangle_m$ and $\langle \cdot \rangle_c$ denote averaging over the domains of the magnet and electrical coil, respectively, $\Omega_m \subset \Omega$ and $\Omega_c \subset \Omega$ denote domains of the magnet and electrical coil, respectively, and $\mathbf{k}$ is the effective stiffness tensor representing electromagnetic interactions. Specifically, $\mathbf{k} = \begin{bmatrix} 0 & 0 \\ 0 & \frac{\kappa I}{A_m} \end{bmatrix}$ in $\Omega_m$ and $\mathbf{k} = \begin{bmatrix} 0 & 0 \\ 0 & \frac{\kappa I}{A_c} \end{bmatrix}$ in $\Omega_c$ in a two-dimensional (2D) plane stress model with $A_m$ and $A_c$ being the areas occupied by the magnet and coil, respectively. Body forces vanish in domains other than the magnet and

electrical coil ($\Omega_o \subset \Omega$). We consider harmonic modulation

$$\mathbf{k} = \mathbf{k}_a \cos(\omega_m t - k_m \langle x \rangle), \tag{4}$$

in which $\mathbf{k}_a$, $\omega_m$, and $k_m$ represent modulation amplitude, modulation frequency, and modulation wavelength, respectively. Due to harmonic modulations, the displacement can be expressed

$$\mathbf{u} = \sum_{p=-\infty}^{+\infty} \mathbf{u}^{(p)}(\mathbf{x}) e^{-i(p\omega_m t + \omega t)}. \tag{5}$$

Substituting Eqs. (2)–(5) into Eq. (1), the $p$th order equations for the three domains read

$$\begin{aligned}
&(\lambda+\mu)\nabla(\nabla\bullet\mathbf{u}^{(p)}) + \mu\nabla^2\mathbf{u}^{(p)} \\
&\quad = -\rho(p\omega_m+\omega)^2\mathbf{u}^{(p)}, \text{ in } \Omega_o, \qquad (6)\\
&(\lambda+\mu)\nabla(\nabla\bullet\mathbf{u}^{(p)}) + \mu\nabla^2\mathbf{u}^{(p)} \\
&\quad + \frac{\mathbf{k}_a e^{-k_m\langle x\rangle}}{2}\left(\left\langle\mathbf{u}^{(p-1)}\right\rangle_c - \left\langle\mathbf{u}^{(p-1)}\right\rangle_m\right) \\
&\quad + \frac{\mathbf{k}_a e^{k_m\langle x\rangle}}{2}\left(\left\langle\mathbf{u}^{(p+1)}\right\rangle_c - \left\langle\mathbf{u}^{(p+1)}\right\rangle_m\right) \\
&\quad = -\rho(p\omega_m+\omega)^2\mathbf{u}^{(p)}, \text{ in } \Omega_m, \qquad (7)\\
&(\lambda+\mu)\nabla(\nabla\bullet\mathbf{u}^{(p)}) + \mu\nabla^2\mathbf{u}^{(p)} \\
&\quad + \frac{\mathbf{k}_a e^{-k_m\langle x\rangle}}{2}\left(\left\langle\mathbf{u}^{(p-1)}\right\rangle_m - \left\langle\mathbf{u}^{(p-1)}\right\rangle_c\right) \\
&\quad + \frac{\mathbf{k}_a e^{k_m\langle x\rangle}}{2}\left(\left\langle\mathbf{u}^{(p+1)}\right\rangle_m - \left\langle\mathbf{u}^{(p+1)}\right\rangle_c\right) \\
&\quad = -\rho(p\omega_m+\omega)^2\mathbf{u}^{(p)}, \text{ in } \Omega_c. \qquad (8)
\end{aligned}$$

The coupling between modes of different orders can be clearly seen in Eqs. (7) and (8). Based on the Bloch theorem, displacements on domain boundaries in one modulation wavelength should satisfy

$$\mathbf{U_l} = e^{ik_x}\mathbf{U_r}, \tag{9}$$

where $k_x$ is the wavenumber along $x$ direction, and $\mathbf{U_l}$ and $\mathbf{U_r}$ are the displacements on the two boundaries. Combining Eqs. (6)–(9) and solving the eigenvalue problem for $\omega$ with given $k_x$, the dispersion relations can be obtained.

In the absence of the modulation (setting $p = 0$), the dispersion relations, $(\omega^{(0)}, k_x^{(0)})$, of free waves propagating in the metamaterial are numerically obtained by the commercial software COMSOL and plotted in Fig. 4(a) (red solid curves), where $a$ denotes the lattice constant (see Appendix A for geometric and material parameters of the design). Scattered waves are expected due to the presence of the spatiotemporal modulation based on the phase matching condition [19]. In Fig. 4(a), only first-order wave modes due to the modulation $(\omega^{(0)} + \omega_m, k_x^{(0)} + k_m)$ and $(\omega^{(0)} - \omega_m, k_x^{(0)} - k_m)$ are plotted in green and purple dotted curves, respectively, to graphically examine the phase matching condition. Phase matching conditions are satisfied at the intersections of those curves, and wave modes are coupled: when one is incident, the others are scattered, modifying wavenumbers and frequencies on dispersion relations. As shown in Fig. 4(a), we identify four simple pairs ($P_1$–$P_4$) of the coupled modes, which are nonsymmetrically distributed to break time-reversal symmetry. For pairs $P_1$ and $P_4$, the two coupled modes propagated along the same direction will interchange their energies [19], whereas, pairs $P_2$ and $P_3$ represent two coupled modes propagating along opposite directions, in which one mode will be transformed

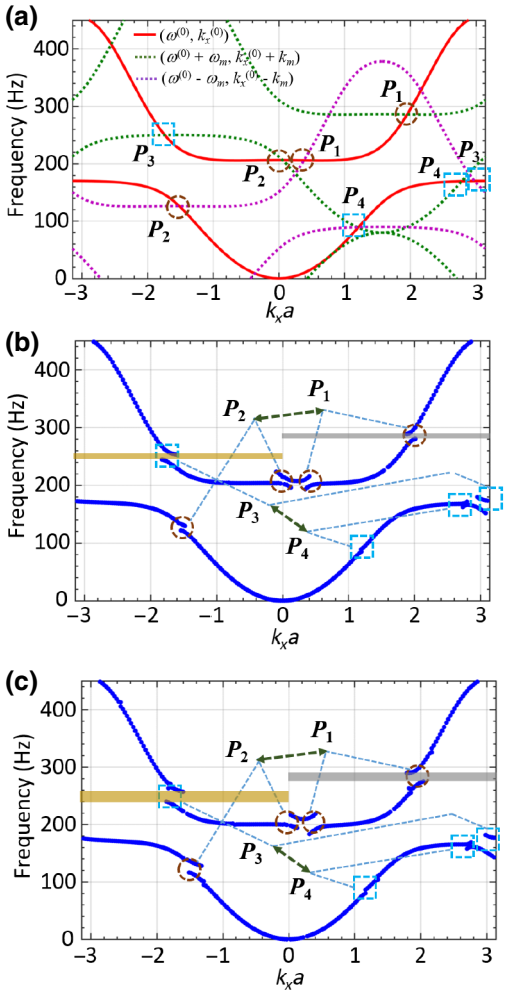


FIG. 4. Dispersion relations of the metamaterial. (a) Dispersion relations of the unmodulated metamaterial (red solid curve) beam and its first-order modes (green and purple dotted curves). (b,c) Dispersion relations of the modulated metamaterial beam calculated with the developed numerical model, where the current amplitude is selected as: (b) 0.25 A, (c) 0.42 A.

to the other mode [19]. Figure 4(b) shows the resulting dispersion relations of the undamped modulated metamaterial according to the developed numerical model, where the pump wave is propagated along the positive $x$ direction with $I_0 = 0.25$ A. The modulation wavenumber and modulation frequency are selected as $\pi/2a$ and 80 Hz, respectively. As illustrated in Fig. 4(b), unidirectional band gaps are clearly seen near those intersections. Attention will be specifically given to frequencies around 170 and 200 Hz, where quad-mode coupling appears. That will generate new nonreciprocities among multiple wave mode conversions, such that simple pairs are unable to remain independent of each other: $P_1$ and $P_2$ are coupled and $P_3$ and $P_4$ are also coupled. As a result, when the incident wave is around 285 Hz (shaded gray area), scattered waves can be translated in both transmitted and reflected domains with frequencies of around 205 and 125 Hz, respectively (dashed circles). However, when the incident wave is around 250 Hz (shaded yellow area), scattered waves can only be found in the reflected domain, but with two different frequencies of around 170 and 90 Hz (dashed squares). Changing the incident direction in both of the two frequency regions will cause the scattered waves to disappear, producing nonreciprocal wave propagation.

## III. EXPERIMENTAL RESULTS

Experimental tests are conducted to demonstrate the nonreciprocal wave propagation in a finite modulated metamaterial beam with 15 unit cells (see Fig. 5). Flexural waves are excited by a shaker fixed on the host beam near the sample. Concentrated 20-peak tone-burst signals with different central frequencies are used to demonstrate nonreciprocal wave propagation at desired frequencies in the modulated metamaterial. To program in space and time the ac input of the coils, modulated electrical signals are generated with the digital controller, amplified by power amplifiers, and finally applied on electrical coils. Two piezoelectric sensors (APC International, Ltd. Material: 850, disk thickness and diameter: 0.25 and 6.5 mm) are bonded on both ends of the metamaterial to measure transmitted and reflected wave signals with a digital oscilloscope. Figures 6(a) and 6(b) show frequency spectra of transmitted and reflected transient waves of the modulated metamaterial for central frequencies at 250 and 285 Hz, respectively. For the purpose of clear comparisons, experimental measurements are plotted in the left column and corresponding numerical simulations are plotted in the right column. The amplitude of the modulation current, $I_0$, is first selected as 0.25 A. Numerical simulations are based on a Rayleigh damping coefficient $\beta_0 = 8 \times 10^{-5}$ s in the cantilever beams [36]. In the figure, "forward or backward" modulation denotes the modulation current travelling in the same or opposite direction as the incident

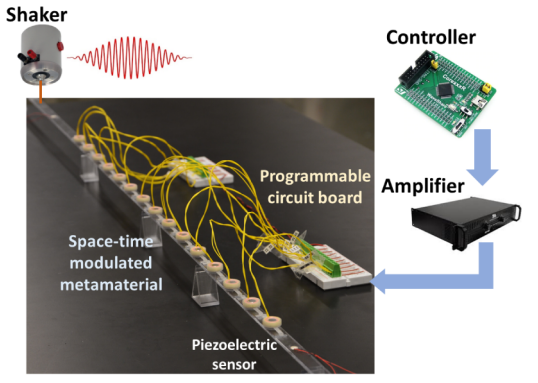


FIG. 5. Experimental setup of the wave transmission test. Flexural waves are generated by a shaker fixed on the host beam near the sample. 20-peak tone-burst signals centered at 250 and 285 Hz are excited in experiments. Two piezoelectric sensors are attached on the host beam to both ends of the metamaterial to measure transmitted and reflected waves, respectively. Modulated currents are generated by a digital controller and amplified with a power amplifier.

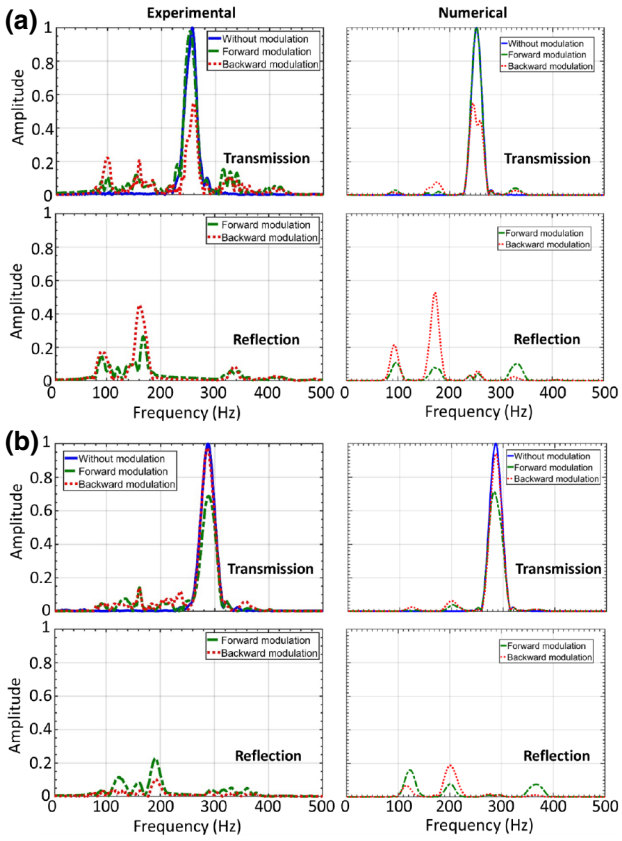


FIG. 6. Nonreciprocal transmission and reflection spectra with $I_0 = 0.25$ A. (a,b) Experimentally measured and corresponding numerically simulated transmitted and reflected wave signals in the frequency domain: (a) the incident wave is centered at 250 Hz, (b) the incident wave is centered at 285 Hz.

flexural wave, which is analogous to a positive or negative wavenumber in Fig. 4(b), respectively. When the tone-burst incident wave is centered at 250 Hz [see Fig. 6(a)], amplitudes of the transmitted wave with the forward modulation are almost the same as those without the modulation, indicating that scattering due to the modulation is negligible; whereas, for the backward modulation, amplitudes of the transmitted wave decay around 250 Hz, demonstrating the unidirectional band-gap behavior [shaded yellow area in Fig. 4(b)]. It is understood that the wave component in the band-gap region is not totally attenuated because the metamaterial is of finite length and the modulation-induced band gap is due to Bragg scattering. In the reflection spectra, two peaks near 170 and 90 Hz are clearly seen when the backward modulation is applied, in agreement with dispersion predictions for unidirectional wave mode conversions in Fig. 4(b). Note that small bumps in transmission as well as reflection spectra with frequency intervals of 80 Hz from 250 Hz are caused by the scattering at interfaces between the host beam and the modulated metamaterial. In the experimental results, noise artifacts are evident at 80 Hz and at its higher harmonics, attributable to tiny misalignments between coils and magnet cylinders. Overall, good agreement between experimental and numerical results is observed.

The nonreciprocal wave propagation is also tested when the central frequency of the incident wave is changed to 285 Hz [see Fig. 6(b)]. It is evident that the transmitted wave amplitudes are unaltered for the metamaterial with the backward modulation. In contrast, amplitudes of the transmitted wave in the metamaterial with the forward modulation are significantly decreased from both numerical and experimental results, demonstrating again the unidirectional band-gap behavior in another frequency region [shaded gray area in Fig. 4(d)]. However, compared with the case in Fig. 6(a), converted wave components in both transmitted and reflected domains are small. To further analyze this behavior, we develop a semianalytical model to calculate transmission and reflection coefficients of the modulated metamaterial beam finite size, $t^{(p)} = w_t^{(p)}/w_0$ and $r^{(p)} = w_r^{(p)}/w_0$ for the mode with the order $p$, where $w_0$, $w_t^{(p)}$, and $w_r^{(p)}$ denote amplitudes of the incident, $p$th order transmitted, and $p$th order reflected waves, respectively (see Appendix B for detailed methods and model validations). This illustrates that in the presence of the material damping in cantilever beams, converted waves for incidence near 285 Hz are almost completely absorbed and the absorption effects due to the material damping are stronger than those for incident near 250 Hz (see Appendix C for details). To better evaluate damping effects, the nonreciprocal energy transport of the modulated metamaterial is quantitatively characterized by the energy bias, $\log_{10}(T_f/T_b)$, where the total transmittances with forward ($f$) and backward ($b$) modulations, $T_f$ and $T_b$, are defined as the summation of each wave mode

$$T_f = \sum_{p=-P}^{+P} \left|t_f^{(p)}\right|^2 \left(\frac{\omega_0 + p\omega_m}{\omega_0}\right)^{5/2},$$
$$T_b = \sum_{p=-P}^{+P} \left|t_b^{(p)}\right|^2 \left(\frac{\omega_0 + p\omega_m}{\omega_0}\right)^{5/2}. \quad (10)$$

Surprisingly, it is found that the largest energy biases occur when small material damping is applied, although the phase matching condition cannot be exactly satisfied. On the other hand, sufficiently large damping coefficients can turn off nonreciprocal wave effects in space-time modulated metamaterials (see Appendix C for details).

To study the effects of the modulation amplitude, Figures 7(a) and 7(b) illustrate frequency spectra of transmitted and reflected transient waves in the modulated metamaterial with modulation amplitude $I_0 = 0.42$ A for the central frequencies 250 and 285 Hz, respectively. Compared with the results in Fig. 6, ($I_0 = 0.25$ A), it is evident

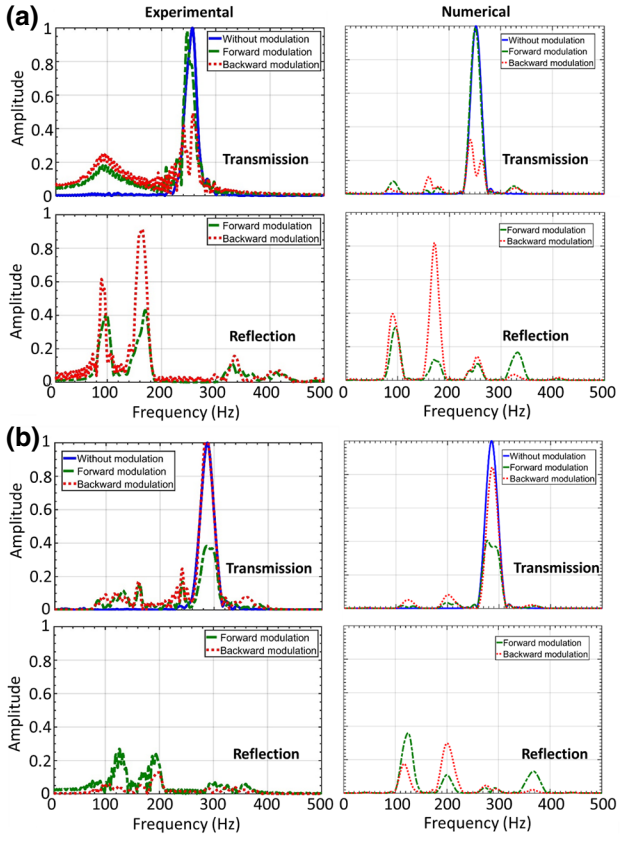


FIG. 7. Nonreciprocal transmission and reflection spectra with $I_0 = 0.42$ A. (a,b) Experimentally measured and corresponding numerically simulated transmitted and reflected wave signals in the frequency domain: (a) the incident wave is centered at 250 Hz, (b) the incident wave is centered at 285 Hz.

that increasing the amplitude of the modulation current leads to stronger nonreciprocity. In particular, the nonreciprocal transmission amplitude bias with forward and backward modulations becomes larger, and the reflected waves caused by the modulation-induced scattering have higher amplitudes, indicating stronger wave mode conversions. This is understandable, as increasing the modulation amplitude is analogous to increasing the scattering mismatch. The observed wave phenomena are also supported by the dispersion relations of the modulated metamaterial with amplitude $I_0 = 0.42$ A [see Fig. 4(c)].

## IV. NONRECIPROCAL TUNABILITY OF THE CONTINUUM-BASED SYSTEM

To fully characterize the nonreciprocal tunability of the system, the defined energy biases are estimated analytically as a function of the modulation amplitude $I_0$ [see Fig. 8(a)], modulation frequency [see Fig. 8(b)], and modulation wavenumber [see Fig. 8(c)]. In the calculation, $\beta_0$ is kept as $8 \times 10^{-5}$ s, and other parameters are also the same as the previous examples. As illustrated in Fig. 8(a), two nonreciprocal frequency regions near 250 ($\log_{10}(T_f/T_b) > 0$) and 285 Hz ($\log_{10}(T_f/T_b) < 0$) are clearly seen, where transmittances are obviously different for forward and backward modulations. Overall, the analytical prediction agrees well with experimental and numerical results from Figs. 6 and 7. As also shown in Fig. 8(a), bandwidths of the two nonreciprocal frequency regions are almost linearly broadened by gradually increasing the amplitude of the modulation current from 0.1 to 0.5 A. To further qualify this linear behavior, the unidirectional band-gap edge frequencies around the intersection are analytically derived based on the perturbation method as (see Appendix D for details)

$$\omega_{\pm} = \omega^{(0)} \pm \frac{\kappa I_0[\omega^{(0)}(\omega^{(0)} - \omega_m)\rho']^2}{2\sqrt{\Lambda_0\Lambda_{-1} - \dfrac{(\Gamma_0\Lambda_{-1} + \Gamma_{-1}\Lambda_0)^2}{4\Gamma_0\Gamma_{-1}}}} \text{ for 250 Hz,} \tag{11}$$

and strong wave conversion frequency boundaries are expressed

$$\omega_{\pm} = \omega^{(0)} \pm \frac{\alpha\kappa I_0[\omega^{(0)}(\omega^{(0)} - \omega_m)\rho']^2}{2\sqrt{\Lambda_0\Lambda_{-1}}} \text{ for 285 Hz,} \tag{12}$$

where $\rho' = m_0/a$, $\omega^{(0)}$ is the frequency at the intersection of dispersion curves [see Fig. 4(a)] and other parameters are detailed in Appendix D. The frequency prediction based on Eqs. (11) and (12) is also plotted in Fig. 8(a) for comparison, especially with stronger modulations. It is clearly illustrated that the nonreciprocal frequency boundaries are indeed proportional to $I_0$.

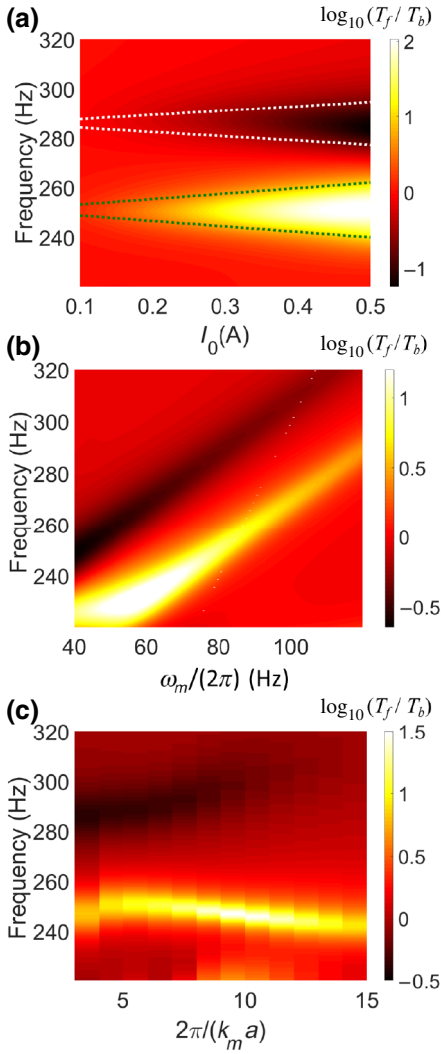


FIG. 8. Nonreciprocal tunability of the modulated metamaterial. (a) Analytically calculated nonreciprocal energy bias of the modulated metamaterial beam with different modulation current amplitudes, where the Rayleigh damping coefficient in cantilevers and the modulation frequency are selected as $8 \times 10^{-5}$ s and 80 Hz, respectively. Dotted lines denote frequency boundaries of nonreciprocal frequency regions calculated based on the perturbation method. (b) Analytically calculated nonreciprocal energy bias of the modulated metamaterial beam with different modulation frequencies, where the Rayleigh damping coefficient in cantilevers remains $8 \times 10^{-5}$ s and $I_0 = 0.25$ A. (c) Analytically calculated nonreciprocal energy bias of the modulated metamaterial beam with different modulation wavenumbers, where the Rayleigh damping coefficient in cantilevers and the modulation frequency are selected as $8 \times 10^{-5}$ s and 80 Hz, respectively, and $I_0 = 0.25$ A.

It is worth mentioning that increasing the modulation amplitude to $I_0 = 0.5$ A will trigger second-order mode coupling $(\omega^{(0)} + 2\omega_m, k_x^{(0)} + 2k_m)$ and $(\omega^{(0)} - 2\omega_m, k_x^{(0)} - 2k_m)$, and scattered waves are then composed of not

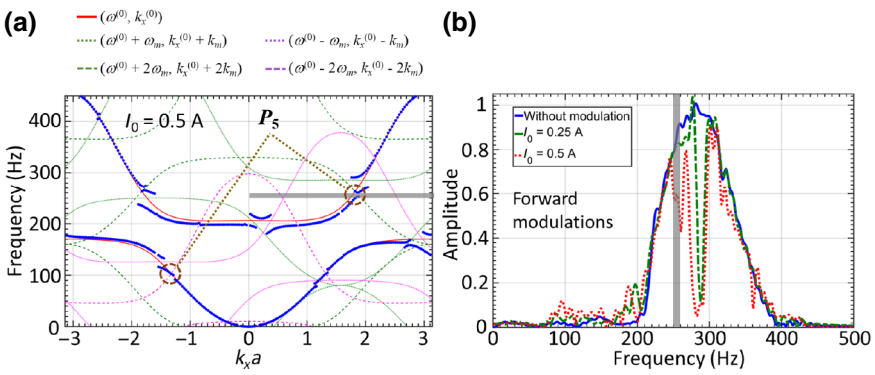


FIG. 9. Unidirectional band gaps induced by higher-order mode interactions. (a) Numerically simulated dispersion relations of an undamped metamaterial beam for modulation current $I_0 = 0.5$ A. Scattering of the second-order mode is observed. (b) Numerically simulated transmission spectra of undamped metamaterial beams with forward modulations, for $I_0 = 0$, 0.25 and 0.5 A.

only the first-order coupling modes, but also the second-order coupling modes. This phenomenon is illustrated in Fig. 9(a): wave dispersion relations are numerically calculated for an undamped metamaterial with modulation current $I_0 = 0.5$ A. Second-order modes, $(\omega^{(0)} + 2\omega_m, k_x^{(0)} + 2k_m)$ and $(\omega^{(0)} - 2\omega_m, k_x^{(0)} - 2k_m)$, are plotted in the figure. The pair, $P_5$, which couples the fundamental and the second-order modes, generates a unidirectional gap near 255 Hz (shaded area) due to the stronger modulation. Wave transmission tests are conducted in an undamped modulated metamaterial beam with 25 unit cells to examine the second-order gap. Figure 9(b) shows the transmission frequency spectra with different forward modulations, where a broader band incident signal is used. Only the first-order gap appears for the modulation current $I_0 = 0.25$ A. Increasing $I_0$ to 0.5 A, the second-order gap is clearly seen (shaded area), which agrees well with the dispersion predictions in Fig. 9(a). Experimental validation of the second-order gap with the current design presents challenges, as the material damping makes the second-order nonreciprocity negligible unless extremely large currents are used.

Besides the modulation amplitude, the modulation frequency is also an important parameter in tuning the nonreciprocity, especially for desired nonreciprocal frequency bands. Figure 8(b) shows nonreciprocal energy biases of the modulated metamaterial beam with different modulation frequencies, where the Rayleigh damping coefficient in resonant beams is kept at $8 \times 10^{-5}$ s and $I_0 = 0.25$ A. Note that the two nonreciprocal bandgap frequency regions are almost linearly shifted with the increase of the modulation frequency and energy biases become smaller at higher frequencies than those at lower frequencies, indicating wave conversion amplitude varies at different frequencies. In Fig. 8(c), the energy biases are calculated analytically with different modulation wavenumbers, $k_m$. In the calculation, the modulation frequency, $I_0$, and $\beta_0$ are kept as 80 Hz, 0.25 A, and $8 \times 10^{-5}$ s, respectively, and other parameters are the same as previous examples. It can be evidenced from the figure that the nonreciprocal frequency region near 285 Hz is slightly shifted to higher frequencies with smaller energy biases when the wavenumber is decreased, and the nonreciprocal behavior almost disappears when $2\pi/(k_m a) > 12$. On the other hand, the nonreciprocal frequency region near 250 Hz first occupies higher frequencies and then gradually shifts to lower frequencies when the wavenumber is decreased, and the largest energy biases are found around $2\pi/(k_m a) = 10$. Finally, it can be concluded that both the nonreciprocal frequency and energy bias can be easily tailored electrically through proper selections of modulation parameters.

## V. DISCUSSION

In summary, we introduce a strategy to design elastic metamaterials with coupling stiffness modulated in space and in time by programmably pumping ac currents into coils and demonstrate, experimentally and theoretically, tunable nonreciprocal flexural wave propagation. The tunability on the wave nonreciprocity is characterized quantitatively in terms of the modulation current amplitude, material damping coefficient, and modulation frequency. The design is compact, robust, and highly flexible in tailoring nonreciprocal frequency regions and wave energy bias ratios. The current method provides a unique configuration that realizes dynamic wave transportation through multiphysical structural response. Our device may open opportunities in structural dynamics and in the design of advanced mechanical insulators, diodes, circulators, and topological insulators.

## ACKNOWLEDGMENTS

This work is supported by the Air Force Office of Scientific Research under Grant No. AF 9550-18-1-0342 with Program Manager Dr. Byung-Lip (Les) Lee and the NSF EFRI under Grant No. 1641078. C.D. acknowledges the support from the NSF EFRI under Grant No. 1741565.

TABLE I. Geometric and material parameters of the metamaterial.

| Host beam (Polycarbonate) | | Resonant beam (RGD 720) | |
|---|---|---|---|
| Young's modulus | 2.6 GPa | Young's modulus | 1.05 GPa |
| Mass density | 1190 kg/m$^3$ | Mass density | 1180 kg/m$^3$ |
| Thickness ($h$) | 2.6 mm | Thickness | 0.6 mm |
| $A$ | 50 mm | $l_b$ | 14 mm |
| $B$ | 14 mm | $w_b$ | 3.5 mm |
| $l_g$ | 1.0 mm | $l_h$ | 3.0 mm |
| Magnet (Neodymium) | | Electromagnet (Coil) | |
| Young's modulus | 160 GPa | Weight | 1.5 g |
| Mass density | 7500 kg/m$^3$ | Height | 4.8 mm |
| Height | 3.2 mm | $D_e$ | 16 mm |
| $d_m$ | 7.9 mm | $D_i$ | 8.2 mm |

## APPENDIX A: GEOMETRIC AND MATERIAL PARAMETERS

Geometric and material parameters of the modulated metamaterial beam are given in Table I. The detailed geometric setup is illustrated in Fig. 10.

## APPENDIX B: SEMI-ANALYTICAL MODELING OF THE MODULATED METAMATERIAL BEAM

We consider a slender beam with periodically attached mass-spring resonators (Fig. 11). The thickness of the beam is denoted by $h$, and the springs in the resonators are modulated in space and in time. The lattice constant and modulation wavelength are represented by $a$ and $L$, respectively. In this study, $N$ mass-spring resonators are contained within one modulation wavelength. Each mass is $m_0$, and the spring constants are represented by $k_1$, $k_2$,... $k_N$ within a modulation wavelength. Material dissipation is defined by the damping constant $c_0$.

According to Euler's beam assumptions, the governing equation of the slender beam can be written as

$$D_0\frac{\partial^4 w(x,t)}{\partial x^4}-\rho_0 h\frac{\partial^2 w(x,t)}{\partial t^2}=\sum_{n=1}^{N}F_n(t)\delta(x-X_n), \quad \text{(B1)}$$

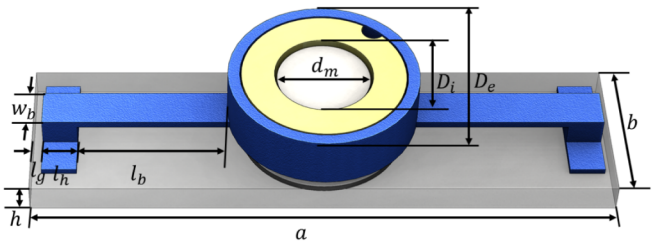


FIG. 10. Schematic of the geometric setup of the metamaterial.

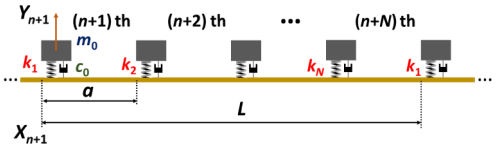


FIG. 11. Schematic of the analytical model of the modulated beam.

where $w$, $D_0$, and $\rho_0$ are the displacement in the vertical direction, bending stiffness, and mass density of the beam, respectively, and the point force $F_n$ due to the attached resonator is

$$F_n(t)=k_n[Y_n(t)-w(X_n,t)]+c_0\left(\frac{\partial Y_n(t)}{\partial t}-\frac{\partial w(X_n,t)}{\partial t}\right)=-m_0\frac{\partial^2 Y_n(t)}{\partial t^2}, \quad \text{(B2)}$$

in which $X_n$ and $Y_n$ denote the coordinate and the vertical displacements of the $n$th resonator, respectively. The modulated spring constants are assumed as

$$k_n=k_0+k_a\cos(\omega_m t-k_m X_n), \quad \text{(B3)}$$

with $\omega_m$, $k_m$, $k_0$, and $k_a$ the modulation frequency, modulation wavenumber, unmodulated stiffness, and amplitude of the modulated stiffness, respectively. It should be noticed that the modulated pumping wave propagates in the positive $x$ direction. Considering the periodicity of the spring constants in time [Eq. (B3)], the local displacement field in the $n$th unit cell can be assumed as

$$w_n(x)=\sum_{p=-\infty}^{+\infty}w_n^{(p)}(x)e^{i(p\omega_m t+\omega t)},\ (n-1)a\le x<na, \quad \text{(B4)}$$

where $w_n^{(p)}$ is the $p$th order displacement. Similarly, the displacement of the masses and point forces applied on the beam can be expressed

$$Y_n(t)=\sum_{p=-\infty}^{+\infty}Y_n^{(p)}e^{i(p\omega_m t+\omega t)}, \quad \text{(B5)}$$

$$F_n(t)=\sum_{p=-\infty}^{+\infty}F_n^{(p)}e^{i(p\omega_m t+\omega t)}. \quad \text{(B6)}$$

Substituting Eq. (B4) into the homogeneous governing beam equation, the general solution of the $p$th order displacement can be found as

$$w_n^{(p)}=A_n^{(p)}e^{ik_p x}+B_n^{(p)}e^{-ik_p x}+C_n^{(p)}e^{k_p x}+D_n^{(p)}e^{-k_p x}, \quad \text{(B7)}$$

where

$$k_p = \left(\frac{\rho_0 h(p\omega_m + \omega)^2}{D_0}\right)^{1/4}.$$

Equation (B3) can be rewritten in exponential form as

$$k_n = k_0 + \frac{k_m(e^{i\omega_m t}e^{-i\phi_n} + e^{-i\omega_m t}e^{i\phi_n})}{2}, \tag{B8}$$

in which $\phi_n = k_m X_n$.

Combining Eqs. (B4), (B5), and (B8) with Eq. (B2), the $p$th order equation of motion for the $n$th mass-spring resonator is obtained as

$$\begin{aligned}&\left[k_0 + ic_0(\omega + p\omega_m) - m_0(\omega + p\omega_m)^2\right] Y_n^{(p)} + \frac{k_m e^{-i\phi_n}}{2} Y_n^{(p-1)} + \frac{k_m e^{i\phi_n}}{2} Y_n^{(p+1)} \\ &= \left[k_0 + ic_0(\omega + p\omega_m)\right]_n^{(p)}(0) + \frac{k_m e^{-i\phi_n}}{2} w_n^{(p-1)}(0) + \frac{k_m e^{i\phi_n}}{2} w_n^{(p+1)}(0).\end{aligned} \tag{B9}$$

It can be found from Eq. (B9) that the displacements of orders $p-1$, $p$, and $p+1$ are coupled with each other due to the modulation. Equation (B9) can also be written in matrix form by truncating the orders of the displacements from $-P$ to $P$ as

$$\mathbf{H_n Y_n} = \mathbf{G_n \bar{W}_n}, \tag{B10}$$

where

$$\mathbf{Y_n} = \left[Y_n^{(-P)} \quad Y_n^{(-P+1)} \quad \dots \quad Y_n^{(0)} \quad \dots \quad Y_n^{(P-1)} \quad Y_n^{(P)}\right]^T,$$

$$\mathbf{\bar{W}_n} = \left[w_n^{(-P)}(0) \quad w_n^{(-P+1)}(0) \quad \dots \quad w_n^{(0)}(0) \quad \dots \quad w_n^{(P-1)}(0) \quad w_n^{(P)}(0)\right]^T.$$

Applying Eq. (B2), the point force vector can then be written as

$$\mathbf{F_n} = \mathbf{J H_n^{-1} G_n \bar{W}_n}, \tag{B11}$$

where

$$\mathbf{F_n} = \left[F_n^{(-P)} \quad F_n^{(-P+1)} \quad \dots \quad F_n^{(0)} \quad \dots \quad F_n^{(P-1)} \quad F_n^{(P)}\right]^T,$$

$$\mathbf{J} = \mathrm{diag}\left(\left[m_0(\omega - p\omega_m)^2 \quad m_0(\omega - (p-1)\omega_m)^2 \quad \dots \quad m_0\omega^2 \quad \dots \quad m_0(\omega + (p-1)\omega_m)^2 \quad m_0(\omega + p\omega_m)^2\right]^T\right).$$

Using Eq. (B7), Eq. (B11) can be rewritten again as

$$\mathbf{F_n} = \mathbf{J H_n^{-1} G_n R A_n}, \tag{B12}$$

where

$$\mathbf{A_n} = \left[A_n^{(-P)} \quad \dots \quad D_n^{(-P)} \quad \dots \quad A_n^{(0)} \quad \dots \quad D_n^{(0)} \quad \dots \quad A_n^{(P)} \quad \dots \quad D_n^{(P)}\right]^T.$$

Continuity conditions on the displacement, rotational angle, bending moment, and shear force are required at $x = X_n$, implying, respectively, for the $p$th displacement

$$\begin{aligned}&A_{n-1}^{(p)} e^{ik_p a} + B_{n-1}^{(p)} e^{-ik_p a} + C_{n-1}^{(p)} e^{k_p a} + D_{n-1}^{(p)} e^{-k_p a} = A_n^{(p)} + B_n^{(p)} + C_n^{(p)} + D_n^{(p)}, \\ &ik_p A_{n-1}^{(p)} e^{ik_p a} - ik_p B_{n-1}^{(p)} e^{-ik_p a} + k_p C_{n-1}^{(p)} e^{k_p a} - k_p D_{n-1}^{(p)} e^{-k_p a} = ik_p A_n^{(p)} - ik_p B_n^{(p)} + k_p C_n^{(p)} - k_p D_n^{(p)}, \\ &-k_p^2 A_{n-1}^{(p)} e^{ik_p a} - k_p^2 B_{n-1}^{(p)} e^{-ik_p a} + k_p^2 C_{n-1}^{(p)} e^{k_p a} + k_p^2 D_{n-1}^{(p)} e^{-k_p a} = -k_p^2 A_n^{(p)} - k_p^2 B_n^{(p)} + k_p^2 C_n^{(p)} + k_p^2 D_n^{(p)}, \\ &-k_p^3 A_{n-1}^{(p)} e^{ik_p a} + k_p^3 B_{n-1}^{(p)} e^{-ik_p a} + k_p^3 C_{n-1}^{(p)} e^{k_p a} - k_p^3 D_{n-1}^{(p)} e^{-k_p a} = -k_p^3 A_n^{(p)} + k_p^3 B_n^{(p)} + k_p^3 C_n^{(p)} - k_p^3 D_n^{(p)} + \frac{F_n^{(p)}}{D_0}.\end{aligned} \tag{B13}$$

Equation (B13) can also be written in matrix form for the vector of displacement from orders $-P$ to $P$, as

$$\mathbf{P_{n-1}A_{n-1}} = \mathbf{Q_nA_n} + \mathbf{VJH_n^{-1}G_nRA_n}. \tag{B14}$$

A local transfer matrix relating $\mathbf{A_{n-1}}$ to $\mathbf{A_n}$ is defined as

$$\mathbf{T_n} = \mathbf{P_{n-1}^{-1}E_n}, \tag{B15}$$

where $\mathbf{E_n} = \mathbf{Q_n} + \mathbf{VJH_n^{-1}G_nR}$. The global transfer matrix covering unit cells within a modulation wavelength can then be expressed

$$\mathbf{T} = \mathbf{T_2T_3} \ldots \mathbf{T_N}, \tag{B16}$$

which satisfies $\mathbf{A_1} = \mathbf{TA_N}$. It can be found from Eq. (B3) that the modulation is also periodic in space. By applying the Bloch theorem, we can write

$$\mathbf{E_1A_1} = e^{ik_xL}\mathbf{P_NA_N}, \tag{B17}$$

where $k_x$ is the wavenumber of the propagating flexural wave. Combining Eqs. (B16) with (B17) gives an eigenvalue system

$$e^{ik_xL}\mathbf{E_1^{-1}P_NA_N} = \mathbf{TA_N}, \tag{B18}$$

from which wavenumbers can be determined for given frequencies. The analytical model is validated by comparing its dispersion relation with the one calculated numerically (Fig. 12). Good agreement can be clearly seen from the figure. Note that moments in small cantilever beams are ignored in this analytical study, which is a valid approximation for frequencies below 400 Hz.

Beside the dispersion calculations, the transfer matrix can also be used to calculate transmission and reflection coefficients, as well as transmittance and reflectance [34], by applying proper boundary conditions.

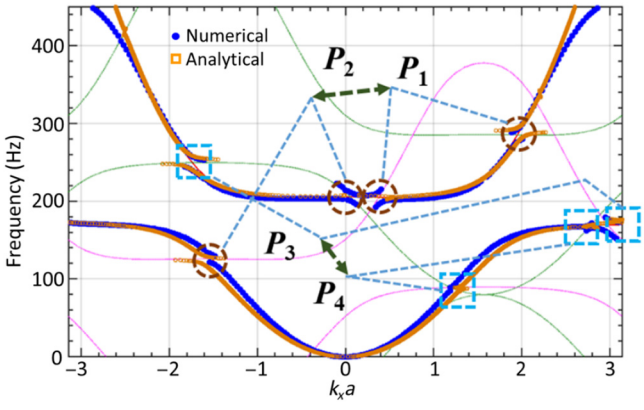


FIG. 12. Comparisons of dispersion relations of the modulated metamaterial beam calculated with the developed numerical and analytical models for a current amplitude of 0.25 A.

## APPENDIX C: EFFECTS OF THE MATERIAL DAMPING

Absolute values of transmission and reflection coefficients of different modes are estimated analytically with $I_0 = 0.25$ A (Fig. 13), where $t_n = w_t^{(n)}/w_0$ and $r_n = w_r^{(n)}/w_0$ where $w_0$, $w_t^{(n)}$ and $w_r^{(n)}$ are the amplitudes of the incident, $n$th order transmitted, and $n$th order reflected waves, respectively. The calculations consider a modulated metamaterial beam with 15 unit cells sandwiched between two infinite host beams. A propagating flexural wave is incident from one infinite host beam to the metamaterial, and transmitted and reflected waves are measured from the other and incident host beams, respectively. We focus on two nonreciprocal regions with incident frequencies at around 250 and 285 Hz. In Fig. 13(a), only strongly coupled modes are illustrated, while other weakly coupled modes are ignored. As shown in Fig. 13(a), $t_0$ has a dip at around 285 Hz when the modulation is forward (shaded area). Due to the mode coupling of the pair $P_1$, energy lost at around 285 Hz is partially scattered to the transmitted wave at around 205 Hz, as a peak appears in $t_{-1}$ at these frequencies (shaded area). This scattered transmitted wave is reflected at boundaries between the metamaterial and the host beam, producing the peak in $r_{-1}$ at around 205 Hz (shaded area). Most importantly, we observe another peak in $r_{-2}$ at around 125 Hz with a much higher amplitude (shaded area), which is caused by the energy exchange between pairs $P_1$ and $P_2$ through the quad-mode coupling at around 205 Hz. This contrasts with previous studies where no energy exchanges between different pairs. $P_1$ and $P_2$ now "communicate." The reflected waves produced by the coupling between pairs as well as reflections at metamaterial boundaries cause the nonreciprocal transmittance for incidence at around 285 Hz. Conversely, for the backward modulation, the incident wave lost at around 250 Hz (a dip in $t_0$, shaded area) is partially scattered to the reflected wave at around 170 Hz (a peak in $r_{-1}$, shaded area), due to the mode coupling of the pair $P_3$. The scattered wave is multiply reflected at metamaterial boundaries and contributes to the peak in $t_{-1}$ at around 170 Hz (shaded area). Due to the coupling between pairs $P_3$ and $P_4$ at around 160 Hz, another peak in $r_{-2}$ appears at around 90 Hz (shaded area). The nonreciprocal transmittance for incidence at around 250 Hz is caused by these reflections.

We now introduce a Rayleigh damping coefficient ($\beta_0 = 8 \times 10^{-5}$ s) in the resonant cantilever beams. The resulting absolute values of transmission and reflection coefficients of different modes are shown in Fig. 13(b). Distinct changes are observed for the transmission and reflection coefficients as compared with the undamped modulated metamaterial. Specifically, the differences in transmission coefficients for forward and backward modulations decrease significantly and the frequency ranges

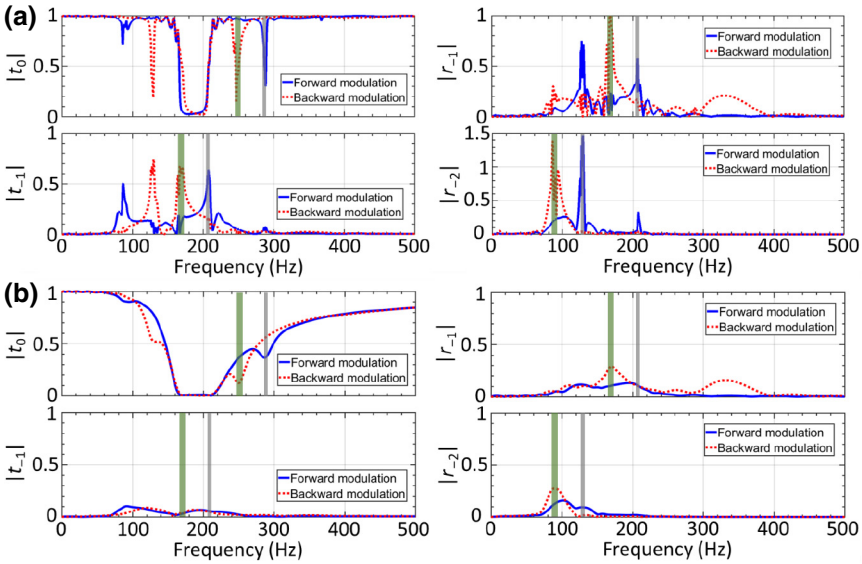


FIG. 13. Analytically calculated absolute values of transmission and reflection coefficients of different modes, for $I_0 = 0.25$ A: (a) Undamped modulated metamaterial beam, (b) damped modulated metamaterial beam, with Rayleigh damping coefficient in resonant beams of $8 \times 10^{-5}$ s.

become much broader. The scattered waves in both the transmitted and reflected domains are markedly suppressed due to the material damping. Two small amplitude scattered waves in the reflected domain are found for the backward modulation with 250-Hz incidence (shaded areas), whereas transmissions and reflections are nearly flat for the forward modulation for 285 Hz incidence (shaded areas), indicating the absorption effects from material damping are stronger than those for incident near 250 Hz.

Finally, in Fig. 14, we consider the effects of material damping on nonreciprocal energy transport in terms of the energy bias for $I_0 = 0.25$ A, with other parameters unchanged. Surprisingly, it shows that the largest energy biases occur for small material damping, although the phase matching condition cannot be fully satisfied, and that sufficiently large damping coefficients can nullify nonreciprocal wave propagation behavior in space-time modulated metamaterials.

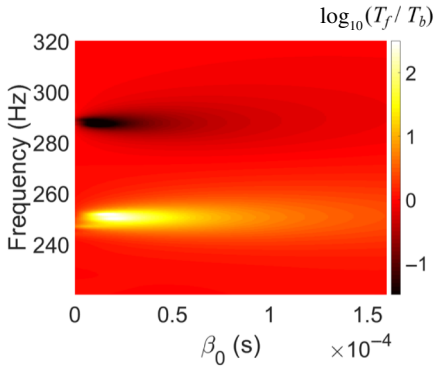


FIG. 14. Analytically calculated nonreciprocal energy bias of a modulated metamaterial beam with different Rayleigh damping coefficients, where $I_0 = 0.25$ A.

## APPENDIX D: NONRECIPROCAL FREQUENCY BOUNDS

The frequency boundaries in the two nonreciprocal frequency regions are estimated based on a perturbation approach, which is demonstrated in this section. Here, we assume the discrete forces from the resonators are continuously distributed along the beam, and governing equations of the beam and its continuous attachments are

$$\rho_0 h \frac{\partial^2 w}{\partial t^2} = \frac{k(t)}{a}(\tilde{w} - w) - D_0 \frac{\partial^4 w}{\partial x^4}, \tag{D1}$$

$$\frac{m_0}{a}\frac{\partial^2 \tilde{w}}{\partial t^2} = \frac{k(t)}{a}(w - \tilde{w}), \tag{D2}$$

where $\tilde{w}$ represents the vertical displacement of continuous attachments and $k(t) = k_0 + k_a \cos(k_m x - \omega_m t)$ with $k_m$ the modulation wavenumber. Equations (D1) and (D2) can be written in matrix form as

$$\mathbf{M}\frac{\partial^2}{\partial t^2}\boldsymbol{\Psi} + \mathbf{K}\psi + \mathbf{D}\frac{\partial^4}{\partial x^4}\boldsymbol{\psi} = \mathbf{0}, \tag{D3}$$

in which

$$\boldsymbol{\psi} = \begin{bmatrix} w & \tilde{w} \end{bmatrix}^T,$$

$$\mathbf{M} = \begin{bmatrix} \rho_0 h & 0 \\ 0 & \dfrac{m_0}{a} \end{bmatrix},$$

$$\mathbf{K} = \begin{bmatrix} \dfrac{k(t)}{a} & -\dfrac{k(t)}{a} \\ -\dfrac{k(t)}{a} & \dfrac{k(t)}{a} \end{bmatrix},$$

$$\mathbf{D} = \begin{bmatrix} D_0 & 0 \\ 0 & 0 \end{bmatrix}.$$

Without the modulation ($k_a = 0$), the solution to Eq. (D3) can be assumed as

$$\mathbf{\Psi} = \mathbf{\Psi} e^{i(qx-\omega t)}, \tag{D4}$$

where $q$ is the wavenumber. The unmodulated dispersion relation is then

$$D_0 q^4 = \left(\rho_0 h + \frac{m_0}{a}\frac{1}{1-\omega^2/\Omega_0^2}\right)\omega^2 \tag{D5}$$

with $\Omega_0^2 = k_0/m_0$.

In the presence of the modulation, we rewrite Eq. (D3) as

$$\mathbf{M}\frac{\partial^2}{\partial t^2}\tilde{\mathbf{\Psi}} + \mathbf{K}\tilde{\mathbf{\Psi}} + \mathbf{D}\frac{\partial^4}{\partial x^4}\tilde{\mathbf{\Psi}} = \mathbf{0}. \tag{D6}$$

According to the Bloch theorem, the solution to Eq. (D6), $\tilde{\mathbf{\Psi}}$, can be written as

$$\tilde{\mathbf{\Psi}} = \tilde{\mathbf{\Psi}}(k_m x - \omega_m t)e^{i(\tilde{q}x-\tilde{\omega}t)}, \tag{D7}$$

where $\tilde{\mathbf{\Psi}}$ is a periodic function and

$$\begin{aligned}\tilde{\mathbf{\Psi}} &= \mathbf{\Psi} + \delta\mathbf{\Psi},\\ \tilde{q} &= q + \delta q,\\ \tilde{\omega} &= \omega + \delta\omega.\end{aligned}$$

Note that $\delta\mathbf{\Psi}$, $\delta q$, and $\delta\omega$ are on the same order of $k_a$. Substituting Eq. (D7) into Eq. (D6), the leading order equation reads

$$\left[\mathbf{M}\left(i\omega + \omega_m\frac{\partial}{\partial\xi}\right)^2 + \mathbf{K} + \mathbf{D}\left(iq + k_m\frac{\partial}{\partial\xi}\right)^4\right]\mathbf{\Psi} = \mathbf{0}, \tag{D8}$$

where $\xi = k_m x - \omega_m t$. With the Fourier expansion, we have

$$\mathbf{\Psi} = \sum_{j=-\infty}^{+\infty}\mathbf{\Psi}_j e^{ij\xi}. \tag{D9}$$

Combining Eqs. (D8) and (D9), the $j$th order Fourier component is governed by

$$[-\mathbf{M}(\omega + j\omega_m)^2 + \mathbf{K} + \mathbf{D}(q + jk_m)^4]\mathbf{\Psi}_j = \mathbf{0}, \tag{D10}$$

with

$$\mathbf{\Psi}_j = \begin{bmatrix}\frac{k_0}{a} - (\omega_0 + j\omega_m)^2 & \frac{k_0}{a}\end{bmatrix}^T.$$

On the other hand, the first-order equation can be expressed

$$\begin{aligned}&\left[\mathbf{M}\left(i\omega + \omega_m\frac{\partial}{\partial\xi}\right)^2 + \mathbf{K} + \mathbf{D}\left(iq + k_m\frac{\partial}{\partial\xi}\right)^4\right]\delta\mathbf{\Psi}\\ &= \left[-2i\delta\omega\left(i\omega + \omega_m\frac{\partial}{\partial\xi}\right)\mathbf{M}\right.\\ &\qquad\left. -4i\delta q\left(iq + k_m\frac{\partial}{\partial\xi}\right)^3\mathbf{D} - \delta\mathbf{K}(\xi)\right]\mathbf{\Psi}.\end{aligned} \tag{D11}$$

Now considering modes $\mathbf{\Psi}_0$ and $\mathbf{\Psi}_j$ are coupled

$$\begin{aligned}&\left(D_0 q_0^4 = \left(\rho_0 h + \frac{m_0}{a}\frac{1}{1-\omega_0^2/\Omega_0^2}\right)\omega_0^2 \text{ and } D_0(q_0 + jk_m)^4\right.\\ &\left. = \left(\rho_0 h + \frac{m_0}{a}\frac{1}{1-(\omega_0 + j\omega_m)}^2/\Omega_0^2\right)(\omega_0 + j\omega_m)^2\right),\end{aligned}$$

and the leading order solution then becomes

$$\mathbf{\Psi} = V_0\mathbf{\Psi}_0 + V_1\mathbf{\Psi}_j, \tag{D12}$$

where $V_0$ and $V_j$ are the amplitudes of the two modes. Similarly, the Fourier expansion can be applied again

$$\delta\mathbf{\Psi} = \sum_{j=-\infty}^{+\infty}\delta\mathbf{\Psi}_j e^{ij\xi}. \tag{D13}$$

Combining Eqs. (D9) and (D11)–(D13), we can derive

$$\begin{aligned}&(-\mathbf{M}\omega_0^2 + \mathbf{K} + \mathbf{D}q_0^2)\delta\mathbf{\Psi}_0\\ &= (2\delta\omega\omega_0\mathbf{M} - 4\delta q q_0^3\mathbf{D})\mathbf{\Psi}_0 V_0 - \delta\bar{\mathbf{K}}_j\mathbf{\Psi}_j V_1,\end{aligned} \tag{D14}$$

$$\begin{aligned}&(-\mathbf{M}\omega_j^2 + \mathbf{K} + \mathbf{D}q_j^2)\delta\mathbf{\Psi}_j\\ &= (2\delta\omega\omega_j\mathbf{M} - 4\delta q q_j^3\mathbf{D})\mathbf{\Psi}_j V_1 - \delta\mathbf{K}_j\mathbf{\Psi}_0 V_0.\end{aligned} \tag{D15}$$

In order to ensure the solutions $\delta\mathbf{\Psi}_0$ and $\delta\mathbf{\Psi}_j$ are bounded, Eqs. (D14) and (D15) should satisfy

$$\mathbf{\Psi}_0(2\delta\omega\omega_0\mathbf{M} - 4\delta q q_0^3\mathbf{D})\mathbf{\Psi}_0 V_0 - \mathbf{\Psi}_0\delta\bar{\mathbf{K}}_j\mathbf{\Psi}_j V_1 = 0, \tag{D16}$$

$$\mathbf{\Psi}_j(2\delta\omega\omega_j\mathbf{M} - 4\delta q q_j^3\mathbf{D})\mathbf{\Psi}_j V_1 - \mathbf{\Psi}_j\delta\mathbf{K}_j\mathbf{\Psi}_0 V_0 = 0. \tag{D17}$$

From Eqs. (D16) and (D17), one can obtain

$$\begin{vmatrix}\delta\omega\Lambda_0 - \delta q\Gamma_0 & -\frac{k_a(\omega_0\omega_j\rho')^2}{2}\\ -\frac{k_a(\omega_0\omega_j\rho')^2}{2} & \delta\omega\Lambda_j - \delta q\Gamma_j\end{vmatrix} = 0, \tag{D18}$$

where

$$\Lambda_{0,j} = 2\omega_{0,j}\left(\rho_0 h\left(\frac{k_0 - \omega_{0,j}^2 m_0}{a}\right)^2 + \rho'\frac{k_0^2}{a^2}\right),$$

$$\Gamma_{0,j} = 4q_{0,j}^3 D_0\left(\frac{k_0 - \omega_{0,j}^2 m_0}{a}\right)^2,$$

with $\omega_j = \omega_0 + j\,\omega_m$ and $q_j = q_0 + j\,q_m$. For the pair coupled with the two modes propagating in opposite directions, a unidirectional frequency band gap would open [18]. The unidirectional band-gap edge frequencies (i.e., near 250 Hz) can be found by imposing [18]

$$\frac{\partial\delta\omega}{\partial\delta q} = 0. \tag{D19}$$

As a result,

$$\omega_\pm = \omega^{(0)} \pm \frac{\kappa I_0[\omega^{(0)}(\omega^{(0)} - \omega_m)\rho']^2}{2\sqrt{\Lambda_0\Lambda_{-1} - \frac{(\Gamma_0\Lambda_{-1} + \Gamma_{-1}\Lambda_0)^2}{4\Gamma_0\Gamma_{-1}}}}. \tag{D20}$$

On the other hand, for the pair coupled with the two modes propagating in the same direction, a unidirectional gap in the wavenumber domain would open [18]. As a result, explicit frequency boundary expressions cannot be easily found. To characterize the strong wave conversion frequency regions for this case (i.e., near 285 Hz), we first find $\delta\omega$ at $\delta q = 0$ and then implement a factor $\alpha$ to estimate those frequency boundaries as

$$\omega_\pm = \omega^{(0)} \pm \frac{\alpha\kappa I_0[\omega^{(0)}(\omega^{(0)} - \omega_m)\rho']^2}{2\sqrt{\Lambda_0\Lambda_{-1}}}. \tag{D21}$$

For the case demonstrated in the main text, $\alpha$ is selected as 0.5.

## APPENDIX E: SAMPLE FABRICATION

The fabrication processes of the sample are shown in Fig. 2. The modulated metamaterial is fabricated by first gluing magnetic cylinders onto 3D printed cylinders (Step 1). The glued samples are then bonded on a surface of a host (polycarbonate) beam with intervals of the lattice constant (Step 2). Subsequently, electrical coils are mounted into the 3D printed holders (Step 3), with each holder containing two cantilever beams. Finally, the ends of cantilever beams are bonded onto the host beam with proper alignments between magnets and coils (Step 4).


[1] J. D. Achenbach, *Reciprocity in Elastodynamics* (Cambridge University Press, Cambridge, UK, 2003).

[2] H. Lamb, On reciprocal theorems in dynamics, Proc. Lond. Math. Soc. **19**, 144 (1888).

[3] R. Fleury, D. L. Sounas, M. R. Haberman, and A. Alù, Nonreciprocal acoustics, Acoust. Today **11**, 14 (2015).

[4] S. A. Cummer, J. Christensen, and A. Alù, Controlling sound with acoustic metamaterials, Nat. Rev. Mater. **1**, 16001 (2016).

[5] R. Fleury, D. L. Sounas, C. F. Sieck, M. R. Haberman, and A. Alù, Sound isolation and giant linear nonreciprocity in a compact acoustic circulator, Science **343**, 516 (2014).

[6] B. Liang, X. S. Guo, J. Tu, D. Zhang, and J. C. Cheng, An acoustic rectifier, Nat. Mater. **9**, 989 (2010).

[7] G. Trainiti and M. Ruzzene, Non-reciprocal elastic wave propagation in spatiotemporal periodic structures, New J. Phys. **18**, 083047 (2016).

[8] K. L. Tsakmakidis, L. Shen, S. A. Schulz, X. Zheng, J. Upham, X. Deng, H. Altug, A. F. Vakakis, and R. W. Boyd, Breaking Lorentz reciprocity to overcome the time-bandwidth limit in physics and engineering, Science **356**, 1260 (2017).

[9] X. F. Li, X. Ni, L. Feng, M. H. Lu, C. He, and Y. F. Chen, Tunable Unidirectional Sound Propagation Through a Sonic-Crystal-Based Acoustic Diode, Phys. Rev. Lett. **106**, 084301 (2011).

[10] N. Boechler, G. Theocharis, and C. Daraio, Bifurcation-based acoustic switching and rectification, Nat. Mater. **10**, 665 (2011).

[11] P. Wang, L. Lu, and K. Bertoldi, Topological Phononic Crystals with One-Way Elastic Edge Waves, Phys. Rev. Lett. **115**, 104302 (2015).

[12] L. M. Nash, D. Kleckner, A. Read, V. Vitelli, A. M. Turner, and W. T. M. Irvine, Topological mechanics of gyroscopic metamaterials, Proc. Natl. Acad. Sci. **112**, 14495 (2015).

[13] Z. Zhang, I. Koroleva, L. I. Manevitch, L. A. Bergman, and A. F. Vakakis, Nonreciprocal acoustics and dynamics in the in-plane oscillations of a geometrically nonlinear lattice, Phys. Rev. E **94**, 032214 (2016).

[14] D. L. Sounas and A. Alù, Non-reciprocal photonics based on time modulation, Nat. Photonics **11**, 774 (2017).

[15] E. Cassedy and A. Oliner, Dispersion relations in time-space periodic media: Part I-stable interactions, Proc. IEEE **51**, 1342 (1963).

[16] E. Cassedy, Dispersion relations in time-space periodic media: Part II-Unstable interactions, Proc. IEEE **55**, 1154 (1967).

[17] N. Swinteck, S. Matsuo, K. Runge, J. O. Vasseur, P. Lucas, and P. A. Deymier, Bulk elastic waves with unidirectional backscattering-immune topological states in a time-dependent superlattice, J. Appl. Phys. **118**, 063103 (2015).

[18] H. Nassar, H. Chen, A. N. Norris, M. R. Haberman, and G. L. Huang, Non-reciprocal wave propagation in modulated elastic metamaterials, Proc. R. Soc. A **473**, 20170188 (2017).

[19] H. Nassar, H. Chen, A. Norris, and G. Huang, Non-reciprocal flexural wave propagation in a modulated metabeam, Extreme Mech. Lett. **15**, 97 (2017).

[20] M. H. Ansari, M. A. Attarzadeh, M. Nouh, and M. A. Karami, Application of magnetoelastic materials in spatiotemporally modulated phononic crystals for

nonreciprocal wave propagation, Smart Mater. Struct. **27**, 015030 (2017).

[21] K. Yi, M. Collet, and S. Karkar, Frequency conversion induced by time-space modulated media, Phys. Rev. B **96**, 104110 (2017).

[22] H. Nassar, X. Xu, A. Norris, and G. Huang, Modulated phononic crystals: Non-reciprocal wave propagation and Willis materials, J. Mech. Phys. Solids **101**, 10 (2017).

[23] S. P. Wallen and M. R. Haberman, Non-reciprocal wave phenomena in spring-mass chains with effective stiffness modulation induced by geometric nonlinearity, Phys. Rev. E **99**, 013001 (2019).

[24] Y. Wang, B. Yousefzadeh, H. Chen, H. Nassar, G. Huang, and C. Daraio, Observation of Nonreciprocal Wave Propagation in a Dynamic Phononic Lattice, Phys. Rev. Lett. **121**, 194301 (2018).

[25] J. Gump, I. Finkler, H. Xia, R. Sooryakumar, W. J. Bresser, and P. Boolchand, Light-Induced Giant Softening of Network Glasses Observed Near the Mean-Field Rigidity Transition, Phys. Rev. Lett. **92**, 245501 (2004).

[26] N. Swinteck, S. Matsuo, K. Runge, J. O. Vasseur, P. Lucas, and P. A. Deymier, Photoplastic effects in chalcogenide glasses: A review, Phys. Status Solids B **246**, 1773 (2009).

[27] F. Casadei, T. Delpero, A. Bergamini, P. Ermanni, and M. Ruzzene, Piezoelectric resonator arrays for tunable acoustic waveguides and metamaterials, J. Appl. Phys. **112**, 064902 (2012).

[28] Y. Y. Chen, G. L. Huang, and C. T. Sun, Band gap control in an active elastic metamaterial with negative capacitance piezoelectric shunting, J. Vib. Acoust. **136**, 061008 (2014).

[29] Y. Y. Chen, R. Zhu, M. V. Barnhart, and G. L. Huang, Enhanced flexural wave sensing by adaptive gradient-index metamaterials, Sci. Rep. **6**, 35048 (2016).

[30] G. Wang, J. Cheng, J. Chen, and Y. He, Multi-resonant piezoelectric shunting induced by digital controllers for subwavelength elastic wave attenuation in smart metamaterial, Smart Mater. Struct. **26**, 025031 (2017).

[31] Y. Y. Chen, G. K. Hu, and G. L. Huang, An adaptive metamaterial beam with hybrid shunting circuits for extremely broadband control of flexural waves, Smart Mater. Struct. **25**, 105036 (2016).

[32] Y. Y. Chen, G. K. Hu, and G. L. Huang, A hybrid elastic metamaterial with negative mass density and tunable bending stiffness, J. Mech. Phys. Solids **105**, 179 (2017).

[33] X. P. Li, Y. Y. Chen, G. K. Hu, and G. L. Huang, A self-adaptive metamaterial beam with digitally controlled resonators for subwavelength broadband flexural wave attenuation, Smart Mater. Struct. **27**, 045015 (2018).

[34] K. Danas, S. V. Kankanala, and N. Triantafyllidis, Experiments and modeling of iron-particle-filled magnetorheological elastomers, J. Mech. Phys. Solids **60**, 120 (2012).

[35] E. J. Reed, M. Soljačić, and J. D. Joannopoulos, Reversed Doppler Effect in Photonic Crystals, Phys. Rev. Lett. **91**, 133901 (2003).

[36] M. Vachon, Dynamic response of 3D printed beams with damping layers (Massachusetts Institute of Technology, Thesis, 2015).